

# SiCN Ceramics as Electrode Materials for Sodium/Sodium Ion Cells – Insights from $^{23}\text{Na}$ In-Situ Solid-State NMR

Edina Šić,<sup>[a]</sup> Marco Melzi d’Eril,<sup>[b]</sup> Konstantin Schutjajew,<sup>[c]</sup> Magdalena J. Graczyk-Zajac,<sup>[b, d]</sup> Hergen Breitzke,<sup>[a]</sup> Ralf Riedel,<sup>[b]</sup> Martin Oschatz,<sup>[c]</sup> Torsten Gutmann,\*<sup>[a]</sup> and Gerd Buntkowsky\*<sup>[a]</sup>

Polymer-derived silicon carbonitride ceramic (SiCN) is used as an electrode material to prepare cylindrical sodium/sodium ion cells for solid-state NMR investigations. During galvanostatic cycling structural changes of the environment of sodium/sodium ions are investigated by applying  $^{23}\text{Na}$  in-situ solid-state NMR. Changes of the signals assigned to sodium metal, intercalated sodium cation and sodium cation originating from the electrolyte are monitored as well as the occurrence of an

additional signal in the region of metallic sodium. The intensity of this additional signal changes periodically with the cycling process indicating the reversibility of structures formed and deformed during the galvanostatic cycling. To identify interactions of sodium/sodium ions with the SiCN electrode materials, the cycled SiCN material is studied by  $^{23}\text{Na}$  ex-situ MAS NMR at high spinning rates of 20 and 50 kHz to obtain appropriate spectral resolution.

## Introduction

In times of increasing digitization, changes of modern information and communication technologies and the ongoing energy revolution from fossil resources to renewable resources, the market requires efficient electrochemical energy storage materials with optimum physical-chemical properties such as high energy density, wide temperature range of operation, fast charging/discharging, long lifetime etc. The shortage of resources and material availability as well as limited recycling processes lead to an increased focus on alternative materials.<sup>[1,2]</sup> The development of cost-effective energy storage systems addressed with an evaluation of sustainable energy technolo-

gies has become a global challenge.<sup>[3,4]</sup> Currently, high performance alkali batteries are one of the key component technologies used in diverse energy storage devices.<sup>[5,6]</sup> The idea of cost-efficient sodium storage systems goes back to the 1960s where the ability of sodium ion transport in sodium- $\beta$ -alumina ( $\text{NaAl}_1\text{O}_1$ ) was discovered,<sup>[7]</sup> leading to promising developments in the following periods, i.e., of the high temperature sodium-sulfur and sodium-nickel chloride batteries.<sup>[8,9]</sup> In the meantime, lithium containing battery systems have been developed and studied in more detail due to their high energy density playing an important role in the stationary, mobile and transportation energy sector.<sup>[10–13]</sup> Many efforts have been made on the improvement of electrode materials as hosts for lithium insertion, particularly using graphite, different carbon nanostructures, disordered carbon and silicon based materials.<sup>[14–17]</sup>

Owing to the criticality of lithium as a resource for lithium-ion battery (LIB) components,<sup>[18]</sup> an active research on the potential of sodium as an abundant and low-cost alternative for sodium-ion battery (SIB) components has started in the past few years.<sup>[9,13,19–23]</sup> Sodium exhibits physical-chemical features comparable to lithium, leading to analogous operating principles with respect to large-scale energy storage applications and makes up ca. 2.6% of the earth crust.<sup>[2,24,25]</sup> Due to the more covalent character of the carbon-lithium bond compared to the carbon-sodium bond and the higher formation energy for  $\text{NaC}_6$  compared to  $\text{LiC}_6$ , the commonly used commercial graphite electrode materials for lithium batteries are less suitable for sodium batteries as charge carrier,<sup>[26,27]</sup> although exfoliated graphite has been addressed in some works.<sup>[13,28,29]</sup> Despite strong efforts in material design to overcome this issue, such as e.g., materials with disordered structure, extrinsic defects and large interlayer distances, such as hard carbons, carbon black, graphene, tin sulfide based compounds and functionalized organic materials, there is still the lack of an efficient electrode

[a] E. Šić, Dr. H. Breitzke, Dr. T. Gutmann, Prof. Dr. G. Buntkowsky  
Eduard Zintl Institute for Inorganic and Physical Chemistry  
Technical University of Darmstadt  
64287 Darmstadt, Germany  
E-mail: gutmann@chemie.tu-darmstadt.de  
gerd.buntkowsky@tu-darmstadt.de

[b] M. Melzi d’Eril, Dr.-Ing. M. J. Graczyk-Zajac, Prof. Dr. R. Riedel  
Department of Materials and Earth Sciences,  
Group of Dispersive Solids  
Technical University of Darmstadt  
64287 Darmstadt, Germany

[c] Dr. K. Schutjajew, Prof. Dr. M. Oschatz  
Institute for Technical Chemistry and Environmental Chemistry  
Friedrich-Schiller-University Jena  
07743 Jena, Germany

[d] Dr.-Ing. M. J. Graczyk-Zajac  
EnBW Energie Baden-Württemberg AG  
Durlacher Allee 93, 76131 Karlsruhe,  
Germany

 Supporting information for this article is available on the WWW under  
<https://doi.org/10.1002/batt.202200066>

 © 2022 The Authors. *Batteries & Supercaps* published by Wiley-VCH GmbH. This is an open access article under the terms of the Creative Commons Attribution Non-Commercial NoDerivs License, which permits use and distribution in any medium, provided the original work is properly cited, the use is non-commercial and no modifications or adaptations are made.

material for commercial sodium based energy storage materials.<sup>[30–40]</sup>

In our previous works<sup>[41]</sup> high reversible lithiation capacity between 486 and 724 mAh g<sup>-1</sup> for polymer-derived ceramics such as silicon carboxide (SiOC) or silicon carbonitride (SiCN) has been found when applied as an electrode. An in-depth study of these micro- and nanostructured ceramics revealed SiO<sub>4-x</sub>C<sub>x</sub>/SiC<sub>x</sub>N<sub>y</sub> moieties, amorphous parts, and free carbon sheet components in the materials.<sup>[42–48]</sup> Hereby, the silicon atoms are tetrahedral surrounded by carbon and oxygen or nitrogen, whereas carbon in segregated phase exhibits sp<sup>2</sup> hybridized bonds. Defects in the structure, edges in the graphene layers as well as the porous structure provide host-sites for ion adsorption and metal intercalation.<sup>[48–51]</sup> Although, such silicon based PDCs have been studied as alternative anode suitable for lithium storage insertion and a corresponding mechanism has been proposed,<sup>[52]</sup> there are only few works addressing the sodium storage.<sup>[53–55]</sup>

In this paper, we briefly investigate the fundamental sodium storage properties of a silicon-based polymer-derived SiCN ceramic (PDCs) as an anode material in a Swagelok-type ex-situ cell setup, before moving to our main target, the <sup>23</sup>Na in-situ solid-state NMR spectroscopy (ssNMR) of the system in cylindrical sodium/sodium ion cells<sup>[56–58]</sup> which enables us to monitor structural changes of the sodium/sodium ion environments and their reversibility during the cycling process in an active cell. To the best of our knowledge, this is for the first time that the sodium storage into the highly porous SiCN ceramics and the structural changes within the SiCN electrode material during the charging and discharging processes are directly monitored in-situ under the active conditions of a cell. A major experimental challenge in the interpretation of the in-situ ssNMR spectra is the broad line-width of the spectral components. Caused by magnetic susceptibility inhomogeneities due to the cell components and quadrupolar and paramagnetic line-broadening, the spectra consist of broad, overlapping resonances.<sup>[58–61]</sup> In order to aid in the chemical assignment of individual spectral components in the in-situ NMR experiment, additional <sup>23</sup>Na ex-situ ssNMR experiments under MAS conditions were performed.<sup>[62]</sup>

The paper focuses on two fundamental issues, namely i) the preparation of consistent cylindrical cells with an internal diameter of 15 mm suitable for reproducible electrochemical performance of sodium on SiCN, and ii) the establishment and prove of local structure changes of the sodium environment within SiCN electrode materials as well as its reversibility behavior during charging and discharging processes.

## Experimental Section

### Material synthesis

To produce the amorphous SiCN ceramics containing 40%–50% carbon, the polymer perhydropolysilazane dissolved in di-n-butyl ether (PHPS in DBE, AZ Electronic Materials) and the carbon source divinyl benzene (DVB, Sigma Aldrich, UK) were used. Approximately, 10 ppm of Pt<sup>(0)</sup>-1,3-divinyl-1,1,3,3-tetramethyldisiloxane,

diluted in xylene (Sigma-Aldrich, UK) (0.06 mL solution) were added as a catalyst. Reflux of the reaction mixture at 120 °C for 6 h enabled hydrosilylation reaction of the DVB with the PHPS and a preceramic intermediate was obtained. The sample was transferred to a Schlenk tube under argon and brought to 250 °C for 3 h with a programmable furnace to enhance the cross-linking. Subsequently the temperature was increased to 1000 °C at a rate of 100 K/h and kept for 3 h to complete the pyrolysis step. After cooling the sample down to room temperature at a rate of 100 K/h the material is ready for further processing which can take place under air.

After pyrolysis, the samples were ground by hand and milled using a zirconia grinding beaker and a rocker mill "MM 400" (Retsch GmbH, Germany) for 1 h with a frequency of 30 Hz. Subsequently the powders were sieved to particle sizes <40 µm. All material preparation steps and storage apart from milling and printing took place under inert conditions in an argon atmosphere in order to prevent oxidation of the samples.<sup>[63]</sup>

### Ex-situ electrochemical cell setup and cycling

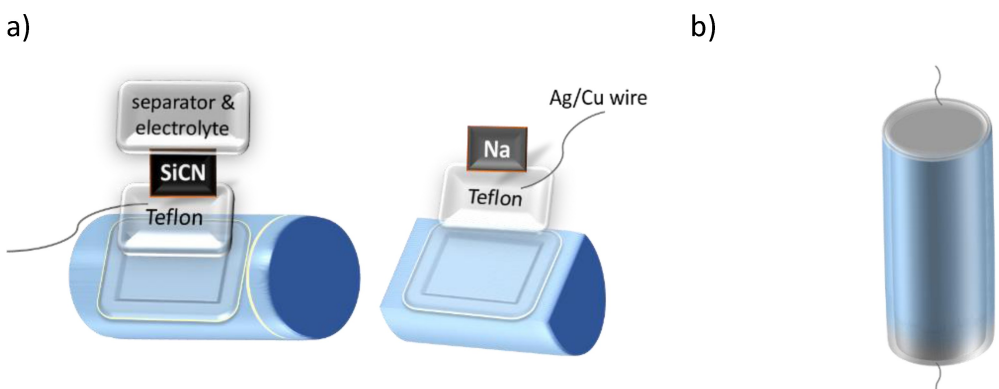
In the first step, 1 g of the ground and sieved (40 µm) SiCN was mixed with an aqueous solution containing 5 wt% of carboxymethylcellulose (CMC, Sigma-Aldrich) to obtain an emulsion. After adding 21.3 mg of carbon black (TIMCAL Super P Conductive Carbon Black) and 53.2 mg of styrene butadiene rubber (SBR, ZEON) the viscosity was adjusted by adding distilled water, and dispersed using an Ultra Turrax T25, to obtain a printable slurry. The slurry was printed on a Cu-foil (9 µm thickness) using a doctor blade set to obtain a film of 125 µm thickness. The foil was dried overnight at 40 °C and subsequently was cut in 10 mm diameter discs. Before being stored in the glovebox, the discs had to undergo another drying process under vacuum which was performed in a Büchi glass tube furnace B-585 for 24 h at 80 °C.

The electrodes were then tested using a Swagelok-type cell in half cell configuration. For this purpose, a metallic sodium (Alfa Aesar Sodium Ingots 99.8%) disc of 10 mm diameter was cut and used as a counter electrode (and also as a reference electrode). A disc cut from a quartz microfiber filter (GE Healthcare Life Sciences, Whatman) of 14 mm diameter was used as a separator. 180 µL of a 1 M solution of NaPF<sub>6</sub> in a 3:7 v/v mixture of ethylene carbonate and diethyl carbonate was dropped on the separator before closing the cell.

The voltage in the system is referred to Na/Na<sup>+</sup> whereas the current density values are referred to the theoretical capacity of the system Li/graphite to provide comparability with the systems in the literature.

### Electrochemical cell setup and cycling

For in-situ solid-state NMR measurements an electrochemical cell (Scheme 1) with a cylindrical shape and an internal diameter of 15 mm was prepared under argon atmosphere keeping the water and oxygen concentration equal or below 0.5 ppm. Serving as the counter electrode, metallic sodium (Sigma-Aldrich) was supported on a copper current collector as well as on a Teflon sheet with a thickness of 0.5 mm providing a densely stacked electrode area. Using a piece of borosilicate glass fiber sheet (Ahlstrom-Munksjö) dried in vacuum at 80 °C, the sodium electrode was separated from the SiCN working electrode. 160 µL of 1 M NaPF<sub>6</sub> electrolyte in ethylene carbonate and diethyl carbonate (EC:DEC 3:7 volume ratio with 5 wt% of fluoroethylene carbonate additive, Xiamen Tob New Energy Technology Co., Ltd) was distributed over the separator uniformly placed on the SiCN side of the cell. To ensure inert conditions inside of the battery and prevent any sodium



**Scheme 1.** a) Illustration of the cell components that were used to prepare the electrochemical cell. The counter electrode (right side) contains sodium which is fixed on a Teflon sheet and connected to an Ag/Cu wire. The working electrode (left side) contains SiCN which is also fixed on a Teflon sheet and connected to an Ag/Cu wire. Between the electrodes a borosilicate glass fiber sheet is used as separator on which the electrolyte was distributed. b) Illustration of the closed cylindrical cell composed of the cell components depicted in a).

oxidation, the external cell capsule was covered with cyanoacrylate glue (Pattex). The rates of the charging and discharging cycles were chosen according to the theoretical specific capacitance of graphite of  $C = 372 \text{ mAh g}^{-1}$ , calculated from the stoichiometry of lithium-graphite intercalation compound Li-GIC (LiC<sub>6</sub>).<sup>[64]</sup> In the in-situ ssNMR studies the prepared cell was initially cycled at a rate of C/10 for ca. 17 h, followed by a slower cycling rate of C/30. The cell charge/discharge was carried out on a Bio-Logic SP-150 cycler using the EC-Lab software version 11.40, employing a voltage variation window between  $-0.03$  and  $2.5 \text{ V}$  vs.  $\text{Na}/\text{Na}^+$ .

### <sup>23</sup>Na in-situ solid-state NMR

<sup>23</sup>Na in-situ solid-state NMR measurements were performed on a Bruker Avance III 300 MHz NMR spectrometer at 7 T corresponding to a frequency of 79.38 MHz for <sup>23</sup>Na. This spectrometer was equipped with a single channel in-situ probe from NMR SERVICE allowing galvanostatic cycling of the cells during solid-state NMR measurements. After assembly, the electrochemical cell was placed in the Ag/Cu coil inside of the probe having a perpendicular orientation with respect to the external static field. Adjustment of the probe resonance circuit conditions during the galvanostatic cycling was performed, recalibrating the carrier frequency automatically by applying a low power continuous wave pulse (0.1 W) to optimize the tuning and matching according to the reflected power. Low-pass filters were connected on the autotune controller inhibiting frequency passages greater than 90 MHz. The <sup>23</sup>Na in-situ NMR spectra were recorded using a laboratory written pseudo 2D solid-echo sequence that includes an autotuning procedure after each single spectrum presented in Figure 1. The pulse lengths in the echo sequence were set to 5  $\mu\text{s}$  at 300 W. The recycle delay was set to 50 ms collecting 15 000 or 30 000 scans per single spectrum. The <sup>23</sup>Na chemical shift was referenced to the signal of an aqueous 1 M NaCl solution (0 ppm).<sup>[65]</sup>

To illustrate changes in the in-situ NMR spectra during the cycling process, each single spectrum was deconvoluted by combined Gauss-Lorentz lines. An example for the deconvolution is given in Supporting Information Figure S8 and Table S1. The relative areas of the metal signal at 1120 ppm ( $A_{r,m}$ ), the shoulder signal at 1128 ppm ( $A_{r,s}$ ), and the electrolyte signal at  $-13 \text{ ppm}$  ( $A_{r,e}$ ) are plotted as function of the time progress of the cycling experiment. They are calculated from the absolute areas  $A_{a,e}$ ,  $A_{a,m}$  and  $A_{a,s}$  according to Equations (1a–c). Note, that the <sup>23</sup>Na in-situ NMR data are only semi-quantitative with respect to the sodium metal content due to the skin depth effect on the metal.

$$A_{r,m} = \frac{A_{a,m}}{A_{a,e} + A_{a,m} + A_{a,s}} \quad (1a)$$

$$A_{r,e} = \frac{A_{a,e}}{A_{a,e} + A_{a,m} + A_{a,s}} \quad (1b)$$

$$A_{r,s} = \frac{A_{a,s}}{A_{a,e} + A_{a,m} + A_{a,s}} \quad (1c)$$

### <sup>23</sup>Na ex-situ solid-state NMR

After 58 h of cycling of the  $\text{Na}|\text{NaPF}_6|\text{SiCN}$  cell, sodium was plated onto SiCN electrode for 10 h at the minimal voltage of  $-0.03 \text{ V}$  vs.  $\text{Na}/\text{Na}^+$  and a current of 20  $\mu\text{A}$ , and then subjected to <sup>23</sup>Na ex-situ MAS NMR measurements. For sample preparation, under an argon atmosphere the electrode material was removed from the copper foil, washed with dimethyl carbonate (Sigma-Aldrich), dried in vacuum, and packed into a 1.3 mm zirconium oxide rotor. <sup>23</sup>Na ex-situ MAS NMR spectra displayed in Figures S7 and 2(a and b) were recorded on a 300 MHz Bruker Avance III HD NMR spectrometer at 7 T corresponding to a frequency of 79.38 MHz for <sup>23</sup>Na, employing a double resonance 1.3 mm <sup>1</sup>H/X probe. The accumulation of 4000 scans was performed at a spinning frequency of 50 kHz by applying the Hahn-echo sequence with  $90^\circ$  and  $180^\circ$  pulses of 1.9  $\mu\text{s}$  and 3.8  $\mu\text{s}$ , respectively, using a recycle delay of 50 ms and a spacing of one rotor period (20  $\mu\text{s}$ ) between the two pulses. The pulse lengths were optimized on  $\text{NaNO}_3$ . The <sup>23</sup>Na chemical shift was referenced to the signal of NaCl powder (7.21 ppm).<sup>[66]</sup> Additional experiments were performed with single pulse excitation to obtain a nutation in the range between 0.2 and 2.0  $\mu\text{s}$ . Each single spectrum in the nutation curve (Figure 2a) was recorded with 1280 scans and a repetition time of 2.5 s. The spectrum shown in Figure 2(b, blue curve) was obtained with a short excitation pulse ( $p_1 = 0.1 \mu\text{s}$ , i.e., flip angle small against  $90^\circ$ ) using a recycle delay of 0.5 s and 81920 accumulations.

<sup>23</sup>Na ex-situ MAS NMR spectra displayed in Figure 2(b and c) were recorded on a 600 MHz Bruker Avance III HD NMR spectrometer at 14.1 T corresponding to a frequency of 158.74 MHz for <sup>23</sup>Na, employing a double resonance 1.3 mm <sup>1</sup>H/X probe. The accumulation of 40960 scans was performed at a spinning frequency of 20 kHz by applying single pulse excitation with short excitation pulse ( $p_1 = 0.1 \mu\text{s}$ , i.e., flip angle small against  $90^\circ$ ) using a recycle

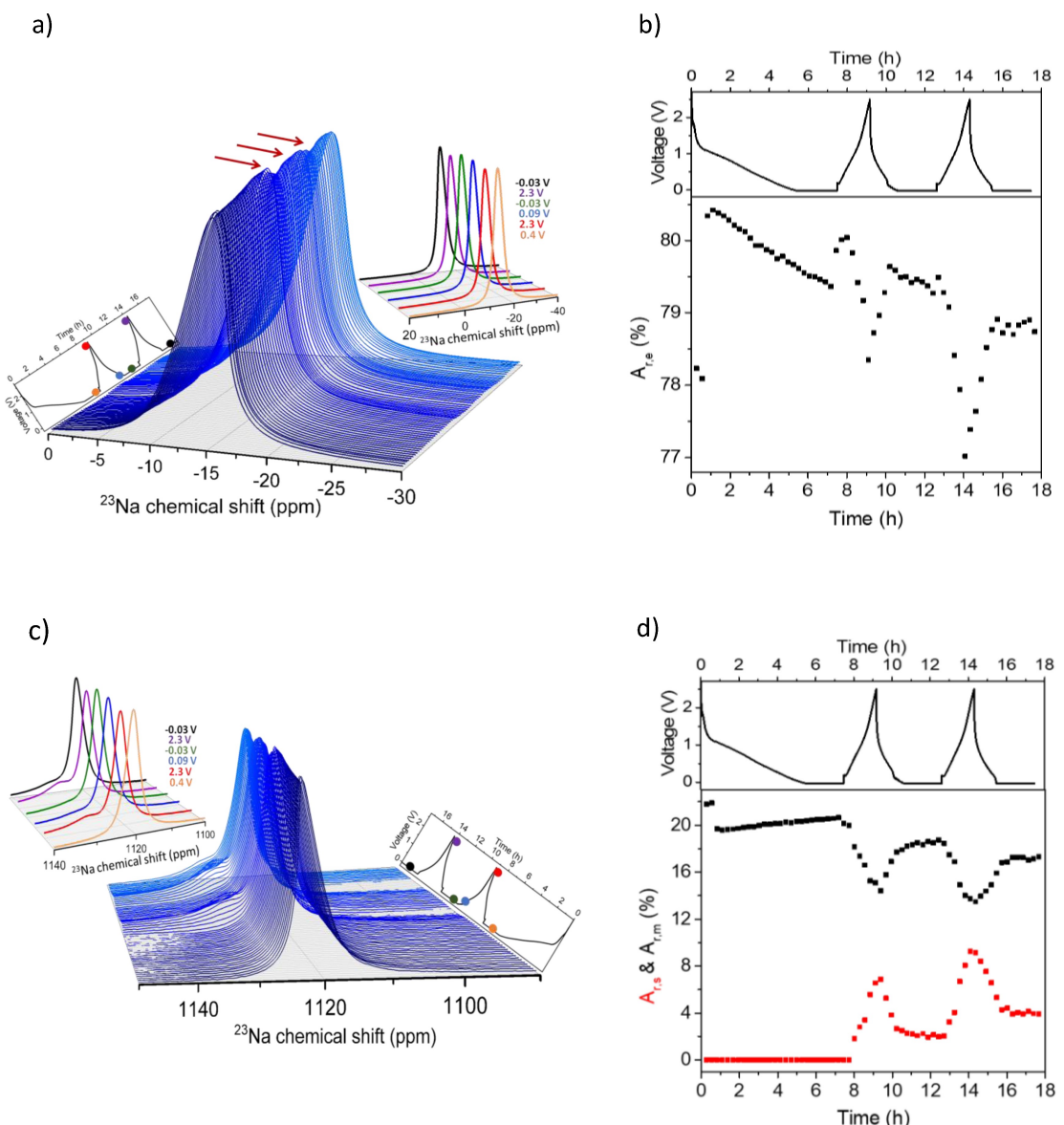


**Figure 1.** a) Enlarged 3D view of the  $^{23}\text{Na}$  in-situ NMR spectra of the electrolyte region (0 to  $-30$  ppm) for the  $\text{Na}|\text{NaPF}_6|\text{SiCN}$  cell. The electrochemical cycling was conducted in the voltage window of  $-0.03$  to  $2.5$  V vs.  $\text{Na}/\text{Na}^+$  applying a current of  $\pm 75$   $\mu\text{A}$  for  $16.56$  h. Extracted  $^{23}\text{Na}$  NMR spectra at various charging stages are shown in the right corner to illustrate intensity fluctuations. b) Relative peak areas  $A_{re}$  of the electrolyte signal obtained by peak deconvolution as a function of the time progress of the cycling experiment. c) Enlarged 3D view of the  $^{23}\text{Na}$  in-situ NMR spectra of the metal region ( $1150$  to  $1090$  ppm) and extracted  $^{23}\text{Na}$  NMR spectra at various charging stages to illustrate changes of the shoulder signal at  $1128$  ppm. d) Relative peak area  $A_{rm}$  for the metal (black curve) and relative peak area  $A_{rs}$  for the shoulder signal (red curve) plotted as a function of time progress of the cycling experiment.

delay of  $0.5$  s. The  $^{23}\text{Na}$  chemical shift was referenced to the signal of  $\text{NaCl}$  powder ( $7.21$  ppm).<sup>[66]</sup>

## Results and Discussion

First insights on the sodiation properties of the PDC material were obtained by performing galvanostatic charge/discharge experiments (Figure S1a) with a current of  $37.2$   $\text{mA g}^{-1}$  and a lower voltage limit of  $-0.03$  V vs.  $\text{Na}/\text{Na}^+$ . The lower limit was set to a value where metallic sodium deposition is expected and was chosen in accordance with previous experiments on Li cells containing the PDC materials.<sup>[52]</sup> In the first cycle a capacity

of  $269$   $\text{mAh g}^{-1}$  was reached, of which  $108$   $\text{mAh g}^{-1}$  could be reversibly cycled. These values indicate the fundamental possibility of anodic sodium storage in PDC ceramics and even more importantly show the prospect of these materials in storing reversibly plated sodium species. Cyclic voltammetry at a scan rate of  $20$   $\mu\text{V s}^{-1}$  (Figure S1b) reveals only one signal during the cathodic scan starting at approximately  $-0.05$  V vs.  $\text{Na}/\text{Na}^+$  with the corresponding anodic signal found at  $0.15$  V vs.  $\text{Na}/\text{Na}^+$ , which is presumably the reverse process of the cathodic peak, according to peak separation and current. The voltage regions more positive than  $0.15$  V vs.  $\text{Na}/\text{Na}^+$  are dominated by a constant current, indicating a process of a capacitive type. From the presence of only one distinguishable

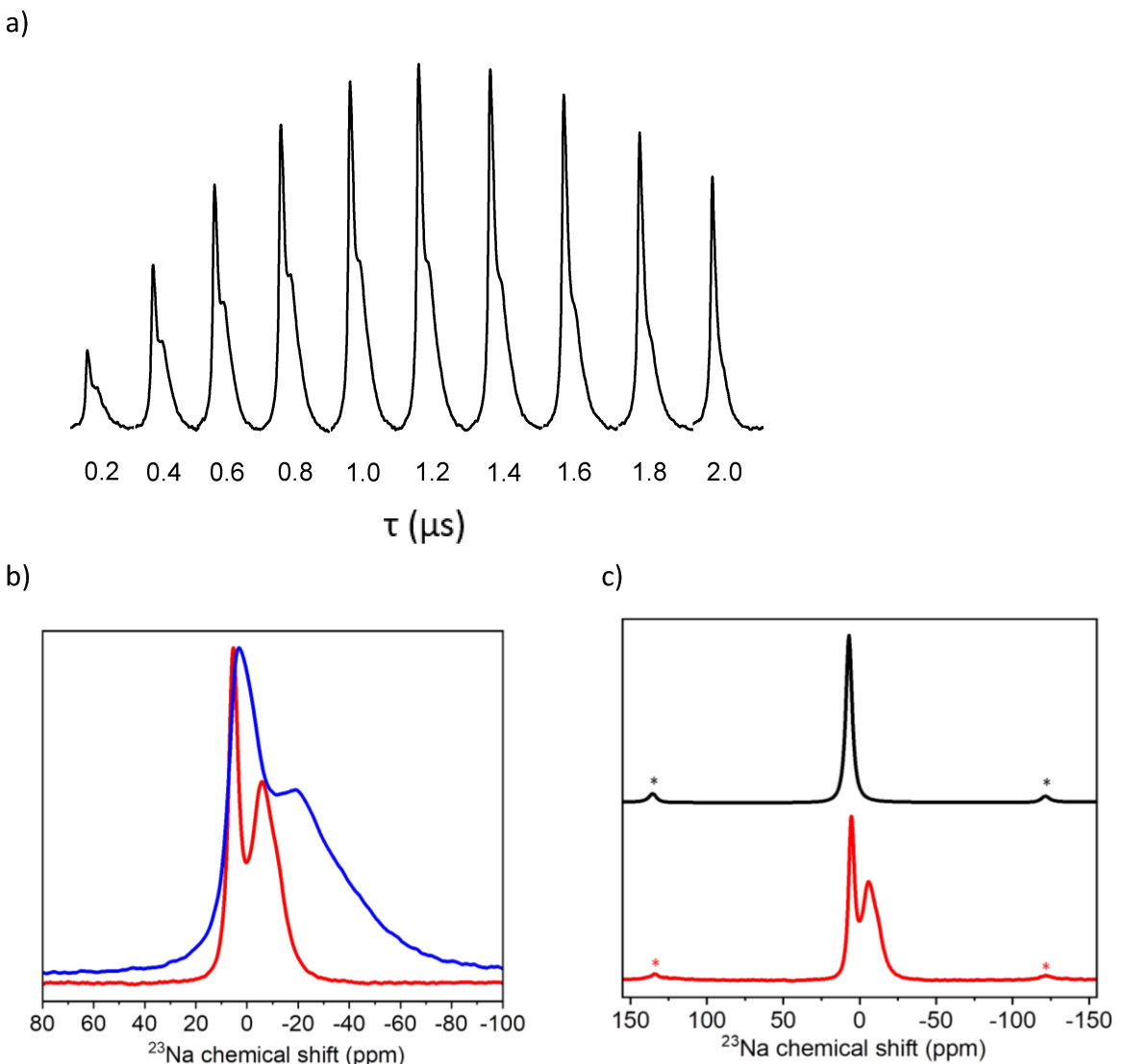


**Figure 2.** a) Nutation curve recorded at 7 T with single pulse excitation for the signal region of the electrolyte signal, showing the different behavior of the narrow and the broad signal. b) Comparison of the  $^{23}\text{Na}$  MAS spectrum of the cycled SiCN obtained at 7 T (blue curve) and at 14.1 T (red curve). c)  $^{23}\text{Na}$  MAS NMR spectra of NaF (black curve) and of the cycled SiCN (red curve) obtained at 14.1 T. Note: Asterisk denotes spinning side bands. Signal enhancement in the  $^{23}\text{Na}$  MAS NMR spectrum of the NaF reference was achieved by applying a  $90^\circ$  pulse of 2.5  $\mu\text{s}$ .

current peak, it can be concluded that most probably only one process is responsible for the sodium storage at the low voltage plateau, which is likely the reversible metal plating, as indicated also by previous results on Li-systems.<sup>[67,68]</sup>

The voltage profile of the  $\text{Na}|\text{NaPF}_6|\text{SiCN}$  cell and an enlarged 3D view of the spectral ranges between 0 and  $-30\text{ ppm}$  as well as between  $1150$  and  $1090\text{ ppm}$  of the corresponding  $^{23}\text{Na}$  in-situ NMR spectra are displayed in Figure 1(a) and (c), respectively. The full spectral range is shown in Figure S2. The  $^{23}\text{Na}$  in-situ NMR spectra show significant changes in the intensity of the signal at around  $-13\text{ ppm}$  (Figure 1a), which is assigned to  $\text{Na}^+$  ions in the electrolyte solution.<sup>[58,60]</sup> Looking at the inset of the  $^{23}\text{Na}$  spectra in Figure 1(a) during the sodiation process (voltage approaches  $-0.03\text{ V}$  vs.  $\text{Na}/\text{Na}^+$ ) no significant change of the intensity of the electrolyte signal is obtained. As the voltage reaches higher

values of up to  $2.5\text{ V}$  vs.  $\text{Na}/\text{Na}^+$  during the desodiation, the intensity of the electrolyte signal decreases significantly. Subsequently, when the voltage goes to the lower cut-off again, the signal intensity returns to the initial state. For the next cycling period, starting at around  $13\text{ h}$ , a similar behavior is noticed. This finding is most probably related to the formation of a solid electrolyte interface (SEI) during the sodiation at higher voltages than  $0.25\text{ V}$  vs.  $\text{Na}/\text{Na}^+$ , while at lower voltages sodiation of free carbon in SiCN most probably starts where sodium intercalates into pores between carbon layers.<sup>[57]</sup> This process should be reversible but is not visible in the  $^{23}\text{Na}$  in-situ spectra, probably due to the quadrupole coupling and paramagnetic interaction of intercalated sodium yielding to broad signals that cannot be resolved under static condition, where the experiments were performed.

Variations of the  $^{23}\text{Na}$  electrolyte signal intensity can be monitored by performing a deconvolution of the in-situ NMR spectra including an integration of the peak areas. In Figure 1(b), the extracted relative area of the electrolyte signal ( $A_{r,e}$ ) is presented as a function of the time progress of the cycling experiment. This progression indicates insignificant changes of  $A_{r,e}$  of about 3%, taking into account that the summation of the peak area is error-prone.

Next to this, the  $^{23}\text{Na}$  in-situ NMR spectra show significant changes in the intensity of the signal at around 1120 ppm (Figure 1c) which corresponds to the sodium metal in the electrochemical cell.<sup>[58,60]</sup> Deeper analysis of the intensity of this signal (Figure 1d, black curve) shows a similar time progress compared to the electrolyte signal. This is again a strong indication for reversibility of processes in the cell. Furthermore, next to the signal at 1120 ppm a shoulder signal at 1128 ppm becomes visible at higher voltages. This new broad signal may be attributed to dendritic sodium deposited at the counter sodium metal electrode.<sup>[59,69]</sup> With increasing voltage of the cell, the shoulder signal rises in intensity (Figure 1d, red curve) suggesting an accumulation of sodium on the metal electrode while decreasing the sodium amount on SiCN. As presented in Figure 1(d, red curve), the relative area  $A_{r,s}$  shows values up to 8% with time progress, whereas the metal peak area  $A_{r,m}$  slopes to a similar value. With decreasing voltage, after the first cycle the shoulder signal disappears and has almost vanished completely (to ca. 2%) at  $-0.03\text{ V}$ .

In the second cycle starting at around 13 h, the shoulder signal at 1128 ppm has reappeared, featuring slightly more pronounced intensity yielding a relative area  $A_{r,s}$  of 10% at the highest voltage of  $2.5\text{ V}$ . This signal has not vanished completely at the lowest voltage of  $-0.03\text{ V}$  vs.  $\text{Na}/\text{Na}^+$  in this cycle where a broad signal with low relative area remained (ca. 4%). This observation indicates the presence of residual dendrites on the sodium metal electrode and "dead" sodium stemming from dendrites that cannot be dissolved completely after the second cycle.

Similar observations have been also noticed on  $\text{Li} \parallel \text{Cu}$  cells where such broad underlying signal components were interpreted as "dead" lithium.<sup>[70]</sup> The formation of "dead" sodium is also visible in further cycles that were performed at lower currents of  $\pm 20\text{ }\mu\text{A}$  as shown in Figures S3–S6. In this case an increase of the area of less than 2% is obtained per cycle. This means that with increasing number of cycles the amount of "dead sodium" increases which may affect the reversibility of the cycling especially when higher currents are applied to the cell.

### $^{23}\text{Na}$ ex-situ MAS NMR

To investigate the sodium storage into SiCN, the sodiated SiCN material was studied by  $^{23}\text{Na}$  ex-situ MAS NMR after disassembling of the cell. In the initially obtained  $^{23}\text{Na}$  MAS Hahn-echo spectrum of the SiCN material at 7 T (see overall spectrum in Figure S7a), signals in the chemical shift range of metallic sodium caused by the galvanostatic cycling are not visible. This

does not necessarily mean that metallic sodium is absent in the sample, since amorphous metallic sodium is most probably invisible in the spectrum due to strong quadrupolar coupling and paramagnetic broadening.

In the chemical shift range of the electrolyte (Figure S7b, red curve), significant changes between the spectrum obtained for the cycled SiCN sample and the SiCN sample wetted with the electrolyte (Figure S7b, black curve) are obtained. In the spectrum of the cycled SiCN, a narrow signal is visible. Next to this signal an overlayed broad shoulder signal becomes visible in the high field region of the spectrum, which is a first hint for various chemical environments of  $^{23}\text{Na}$  stored in SiCN material.

To shed more light on the origin of the narrow and the broad signal, additional  $^{23}\text{Na}$  MAS NMR nutation experiments were performed with single pulse excitation. To investigate the dependence of the spectral line-shape on the excitation pulse length, the nutation curve was recorded for pulse lengths in the range between 0.2 and  $2.0\text{ }\mu\text{s}$ . As can be seen in Figure 2(a), the intensity of the broad signal drops down faster than for the narrow signal. Furthermore, the broad signal changes its shape with increasing pulse length. This observation indicates that the broad signal refers to species with large quadrupolar coupling which cannot be fully excited when the rf field strength  $B_1$  becomes smaller than the quadrupolar coupling  $\omega_Q$  for these species.

In particular, as shown in Figure S7(c), for very short pulse lengths of 0.1 and  $0.2\text{ }\mu\text{s}$  the excitation of both the narrow and the broad signal is homogeneous. This does not seem to be the case for larger pulse lengths where the shape of the broad signal significantly changes. From these observations it is assumed that the sodium species referring to the broad signal have large quadrupolar couplings. This indicates that these species are in unsymmetric environment as this would be the case inside the disordered free carbon structures present in the SiCN ceramic. The narrow signal has a smaller quadrupolar coupling since its shape does not change over a large range of pulse lengths. This is a hint for sodium species in higher symmetric environments, probably sodium ions that are close to the surface of the SiCN material. Sodium ions from free electrolyte can be excluded for this sample since comparison with a freshly prepared SiCN sample wetted with the electrolyte solution shows a significant different chemical shift for the sodium in the electrolyte (about  $-21\text{ ppm}$ ) as illustrated Figure S7(b, black curve).

To obtain more details on the origin of the narrow and broad line, additional  $^{23}\text{Na}$  MAS NMR experiments were performed at a higher field of  $14.1\text{ T}$ . The comparison of the spectrum obtained at  $14.1\text{ T}$  with the one obtained at 7 T is shown in Figure 2(b). As clearly visible, the spectral line-shape strongly depends on the external magnetic field, which is most probably related to effects of the second order quadrupolar interaction leading to a strong broadening of signals at lower magnetic fields. With the current data a deeper line shape analysis is not feasible, since also at  $14.1\text{ T}$  effects of second order quadrupolar interactions cannot be excluded. To overcome this issue, ultra-high field solid-state NMR, or multi-quantum NMR experiments ( $^{23}\text{Na}$  MQMAS) necessitating the

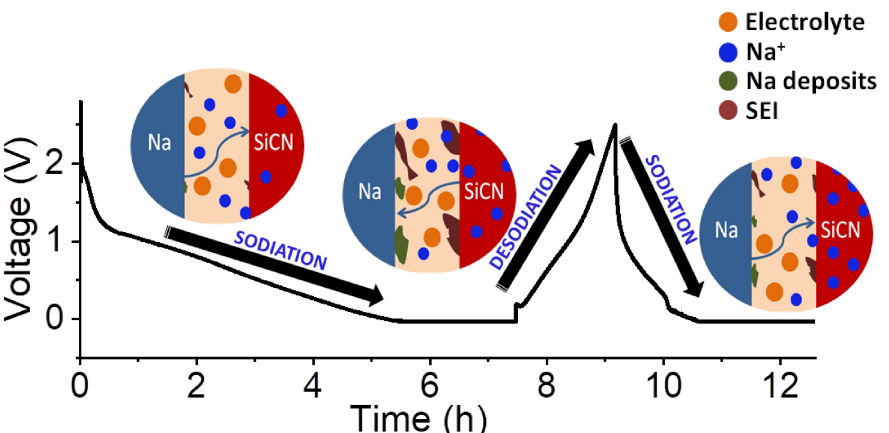


**Figure 3.** Schematic representation of the structural findings of the  $\text{Na}|\text{NaPF}_6|\text{SiCN}$  cell, determined by means of the  $^{23}\text{Na}$  NMR spectra during the sodiation/desodiation process in the voltage window of  $-0.03$  to  $2.5$  V vs.  $\text{Na}/\text{Na}^+$ . During the first sodiation, mobile sodium ion movement to the SiCN electrode is depicted and the appearance of the SEI formation and the sodium electrodeposition is indicated. During the desodiation, the formed SEI and the sodium deposits such as dendrites and “dead sodium” are obtained, whose amount is decreased during the second sodiation process. Hereby, reaching a lower voltage of  $-0.03$  V vs.  $\text{Na}/\text{Na}^+$  the sodium ion adsorption on micropores is assumed to take place as well the sodium storage near to carbon layers.

manufacturing of a larger amount of cycled SiCN have to be performed, which is beyond the scope of the present work. A tentative assignment can be derived from the literature. The narrow line at around 5 ppm is most probably related to  $\text{NaF}$  as suggested by Goward and co-workers<sup>[71]</sup> who analyzed electrochemical reaction products from sodium-oxygen cells and obtained the signal of  $\text{NaF}$  in this spectral region. This  $\text{NaF}$  seems to be in distorted environment as underlined by comparison with the  $^{23}\text{Na}$  reference spectrum of neat  $\text{NaF}$  (Figure 2c). This assignment is further supported by comparison of the  $^{19}\text{F}$  ex-situ MAS spectra in Figure S10. According to Goward and co-workers<sup>[71]</sup> the broad line in the spectrum most probably refers to sodium carbonate which has a quite large quadrupolar coupling constant. Alternatively, this signal may refer to  $\text{Na}^+$  in close vicinity to carbon layers and  $\text{Na}^+$  adsorbed on micropores according to Gotoh et al.<sup>[57]</sup>.

## Conclusion

For the first time, the sodium storage in carbon-rich SiCN composites used as electrodes in sodium/sodium ion cells has been investigated using a combination of  $^{23}\text{Na}$  in-situ and ex-situ solid-state NMR. The  $^{23}\text{Na}$  in-situ NMR results suggest structural changes inside of the SiCN during galvanostatic cycling since intensity fluctuations of the electrolyte signal at  $-13$  ppm and of the sodium metal signal at  $1120$  ppm are clearly visible. In addition, with increasing voltage up to  $2.5$  V, the appearance of a shoulder signal at  $1128$  ppm is observed. This signal is attributed to the formation of dendritic sodium on the sodium metal counter electrode. Such process seems to be reversible to a large extent as it appears/disappears during the sodiation/desodiation which is schematically illustrated in Figure 3. However, the signal does not vanish completely, and a broad signal is persevered at the minimal potential indicating residual sodium electrodeposition and the formation of “dead” sodium. To inspect the sodium storage in SiCN material,  $^{23}\text{Na}$

ex-situ MAS NMR experiments have been performed at  $7$  T and at  $14.1$  T employing spinning rates of  $50$  kHz and  $20$  kHz, respectively. Analysis of the dependency of the line shape on the magnetic field strength and on the flip angle demonstrated that after galvanostatic sodiation the SiCN material contains sodium ions in highly distorted geometry, i.e.,  $\text{Na}^+$  in close vicinity to carbon layers and  $\text{Na}^+$  adsorbed on micropores. Furthermore, the formation of  $\text{NaF}$  during the galvanostatic cycling is indicated. In summary, our studies have demonstrated that SiCN composite materials are suitable for sodium storage and therefore appear to be attractive as anode material in sodium/sodium ion cells.

## Acknowledgements

Financial support is gratefully acknowledged by the EU project SIMBA (Sodium-Ion and Sodium Metal Batteries for efficient and sustainable next-generation energy storage) under grant agreement number 963542. MGZ acknowledges DFG support in the frame of the project GR 4440/4-1. We thank Dr. Oliver Pecher from NMR SERVICE for technical support setting up the in-situ NMR probe. Open Access funding enabled and organized by Projekt DEAL.

## Conflict of Interest

The authors declare no conflict of interest.

## Data Availability Statement

The data that support the findings of this study are available in the supplementary material of this article.

**Keywords:** electrochemical storage • in-situ • SiCN ceramics • sodium • solid-state NMR

- [1] D. H. S. Tan, P. Xu, Z. Chen, *MRS Energy Sustain.* **2020**, 7.
- [2] C. Delmas, *Adv. Energy Mater.* **2018**, 8, 1703137.
- [3] L. Yao, B. Yang, H. Cui, J. Zhuang, J. Je, J. Xue, *J. Mod. Power Syst. Clean Energy* **2016**, 4, 519.
- [4] T. A. Faunce, J. Prest, D. Su, S. J. Hearne, F. Iacopi, *MRS Energy Sustain.* **2018**, 5.
- [5] M. K. Aslam, M. Xu, *Nanoscale* **2020**, 12, 15993.
- [6] T. Famprakis, P. Canepa, J. A. Dawson, M. S. Islam, C. Masquelier, *Nat. Mater.* **2019**, 18, 1278.
- [7] J. Yung-Fan Yu Yao, *J. Inorg. Nucl. Chem.* **1967**, 29, 2453.
- [8] M. S. Whittingham, *Chem. Rev.* **2020**, 120, 6328.
- [9] K. B. Hueso, M. Armand, T. Rojo, *Energy Environ. Sci.* **2013**, 6, 734.
- [10] A. M. Divakaran, D. Hamilton, K. N. Manjunatha, M. Minakshi, *Energies* **2020**, 13, 1477.
- [11] M. S. Whittingham, *Proc. IEEE* **2012**, 100, 1518.
- [12] A. Manthiram, *J. Phys. Chem. Lett.* **2011**, 2, 176.
- [13] N. Yabuuchi, K. Kubota, M. Dahbi, S. Komaba, *Chem. Rev.* **2014**, 114, 11636.
- [14] P. Roy, S. K. Srivastava, *J. Mater. Chem. A* **2015**, 3, 2454.
- [15] S. Xin, Y.-G. Guo, L.-J. Wan, *Acc. Chem. Res.* **2012**, 45, 1759.
- [16] A. R. Kamali, D. J. Fray, *J. New Mater. Electrochem. Syst.* **2010**.
- [17] B. Zhang, C. M. Ghimbeu, C. Laberty, C. Vix-Guterl, J.-M. Tarascon, *Adv. Energy Mater.* **2016**, 6, 1501588.
- [18] P. Greim, A. A. Solomon, C. Breyer, *Nat. Commun.* **2020**, 11, 4570.
- [19] W.-J. Li, S.-L. Chou, J.-Z. Wang, H.-K. Liu, S.-X. Dou, *Nano Lett.* **2013**, 13, 5480.
- [20] C. Jiang, Y. Fang, W. Zhang, X. Song, J. Lang, L. Shi, Y. Tang, *Angew. Chem.* **2018**, 130, 16608.
- [21] I. Landa-Medrano, C. Li, N. Ortiz-Vitoriano, I. Ruiz de Larramendi, J. Carrasco, T. Rojo, *J. Phys. Chem. Lett.* **2016**, 7, 1161.
- [22] H. Wang, E. Matios, J. Luo, W. Li, *Chem. Soc. Rev.* **2020**, 49, 3783.
- [23] B. Sun, P. Xiong, U. Maitra, D. Langsdorf, K. Yan, C. Wang, J. Janek, D. Schröder, G. Wang, *Adv. Mater.* **2020**, 32, e1903891.
- [24] L. Shi, T. Zhao, *J. Mater. Chem. A* **2017**, 5, 3735.
- [25] B. Dunn, H. Kamath, J.-M. Tarascon, *Science* **2018**, 334, 928.
- [26] Y. Wen, K. He, Y. Zhu, F. Han, Y. Xu, I. Matsuda, Y. Ishii, J. Cumings, C. Wang, *Nat. Commun.* **2014**, 5, 4033.
- [27] H. Moriwake, A. Kuwabara, C. A. J. Fisher, Y. Ikuhara, *RSC Adv.* **2017**, 7, 36550.
- [28] P. A. B. Jache, *Angew. Chem. Int. Ed.* **2014**, 53, 10169.
- [29] Y. Li, Y. Lu, P. Adelhelm, M.-M. Titirci, Y.-S. Hu, *Chem. Soc. Rev.* **2019**, 48, 4655.
- [30] P. Lu, Y. Sun, H. Xiang, X. Liang, Y. Yu, *Adv. Energy Mater.* **2018**, 8, 1702434.
- [31] Y. Zhang, X. Li, P. Dong, G. Wu, J. Xiao, X. Zeng, Y. Zhang, X. Sun, *ACS Appl. Mater. Interfaces* **2018**, 10, 42796.
- [32] K. Hong, L. Qie, R. Zeng, Z. Yi, W. Zhang, D. Wang, W. Yin, C. Wu, Q. Fan, W. Zhang, Y. Huang, *J. Mater. Chem. A* **2014**, 2, 12733.
- [33] R. Alcantara, J. M. Jimenez-Mateos, P. Lavelaa, J. L. Tiradoa, *Electrochim. Commun.* **2001**.
- [34] W. Xiao, Q. Sun, J. Liu, B. Xiao, P.-A. Glans, J. Li, R. Li, J. Guo, W. Yang, T.-K. Sham, X. Sun, *Nano Res.* **2017**, 10, 4378.
- [35] J. Pan, S. Chen, Q. Fu, Y. Sun, Y. Zhang, N. Lin, P. Gao, J. Yang, Y. Qian, *ACS Nano* **2018**, 12, 12869.
- [36] S. Anwer, Y. Huang, B. Li, B. Govindan, K. Liao, W. J. Cantwell, F. Wu, R. Chen, L. Zheng, *ACS Appl. Mater. Interfaces* **2019**, 11, 22323.
- [37] G. K. Veerasubramani, M.-S. Park, J.-Y. Choi, D.-W. Kim, *ACS Appl. Mater. Interfaces* **2020**, 12, 7114.
- [38] B. C. Patra, S. K. Das, A. Ghosh, A. Raj K, P. Moitra, M. Addicoat, S. Mitra, A. Bhaumik, S. Bhattacharya, A. Pradhan, *J. Mater. Chem. A* **2018**, 6, 16655.
- [39] D. Luo, J. Xu, Q. Guo, L. Fang, X. Zhu, Q. Xia, H. Xia, *Adv. Funct. Mater.* **2018**, 28, 1805371.
- [40] X.-F. Luo, C.-H. Yang, Y.-Y. Peng, N.-W. Pu, M.-D. Ger, C.-T. Hsieh, J.-K. Chang, *J. Mater. Chem. A* **2015**, 3, 10320.
- [41] L. M. Reinold, M. Graczyk-Zajac, Y. Gao, G. Mera, R. Riedel, *J. Power Sources* **2013**, 236, 224.
- [42] A. Saha, R. Raj, D. L. Williamson, *J. Am. Ceram. Soc.* **2006**, 89, 2188–2195.
- [43] R. Bhandavat, Z. Pei, G. Singh, *Nanomater. Energy* **2012**, 1, 324.
- [44] R. Kolb, C. Fasel, V. Liebau-Kunzmann, R. Riedel, *J. Eur. Ceram. Soc.* **2006**, 26, 3903.
- [45] S. Mukherjee, Z. Ren, G. Singh, *J. Phys. D* **2018**, 51, 463001.
- [46] Y. Feng, S. Dou, Y. Wei, Y. Zhang, X. Song, X. Li, V. S. Battaglia, *ACS Omega* **2017**, 2, 8075.
- [47] G. Shao, D. A. H. Hanaor, J. Wang, D. Kober, S. Li, X. Wang, X. Shen, M. F. Bekheet, A. Gurlo, *ACS Appl. Mater. Interfaces* **2020**, 12, 46045.
- [48] G. Mera, A. Navrotsky, S. Sen, H.-J. Kleebe, R. Riedel, *J. Mater. Chem. A* **2013**, 1, 3826.
- [49] E. Ionescu, H.-J. Kleebe, R. Riedel, *Chem. Soc. Rev.* **2012**, 41, 5032.
- [50] M. Li, L. Cheng, F. Ye, C. Zhang, J. Zhou, *J. Adv. Ceram.* **2021**, 10, 1256.
- [51] M. Graczyk-Zajac, L. M. Reinold, J. Kaspar, P. V. W. Sasikumar, G.-D. Soraru, R. Riedel, *Nanomaterials* **2015**, 5, 233.
- [52] M. Graczyk-Zajac, M. Wimmer, Y. Xu, G. Buntkowsky, C. Neumann, R. Riedel, *J. Solid State Electrochem.* **2017**, 21, 47.
- [53] X. Dou, D. Buchholz, M. Weinberger, T. Diemant, M. Kaus, S. Indris, R. J. Behm, M. Wohlfahrt-Mehrens, S. Passerini, *Small Methods* **2019**, 3, 1800177.
- [54] J. Kaspar, M. Storch, C. Schitko, R. Riedel, M. Graczyk-Zajac, *J. Electrochem. Soc.* **2016**, 163, A156–A162.
- [55] C. Chandra, H. S. Cahyadi, S. Alvin, W. Devina, J.-H. Park, W. Chang, K. Y. Chung, S. K. Kwak, J. Kim, *Chem. Mater.* **2020**, 32, 410.
- [56] Y. Xiang, G. Zheng, Z. Liang, Y. Jin, X. Liu, S. Chen, K. Zhou, J. Zhu, M. Lin, H. He, J. Wan, S. Yu, G. Zhong, R. Fu, Y. Li, Y. Yang, *Nat. Nanotechnol.* **2020**, 15, 883.
- [57] K. Gotoh, *Batteries & Supercaps* **2021**, 4, 1267.
- [58] O. Pecher, P. M. Bayley, H. Liu, Z. Liu, N. M. Trease, C. P. Grey, *J. Magnetic Resonance* **2016**, 265, 200.
- [59] K. Gotoh, T. Yamakami, I. Nishimura, H. Kometani, H. Ando, K. Hashi, T. Shimizu, H. Ishida, *J. Mater. Chem. A* **2020**, 8, 14472.
- [60] P. M. Bayley, N. M. Trease, C. P. Grey, *J. Am. Chem. Soc.* **2016**, 138, 1955.
- [61] J. M. Stratford, P. K. Allan, O. Pecher, P. A. Chater, C. P. Grey, *Chem. Commun.* **2016**, 52, 12430.
- [62] A. I. Freytag, A. D. Pauric, S. A. Krachkovskiy, G. R. Goward, *J. Am. Chem. Soc.* **2019**, 141, 13758.
- [63] M. Storch, D. Vrankovic, M. Graczyk-Zajac, R. Riedel, *Solid State Ionics* **2018**, 315, 59.
- [64] Y. Nishi, *J. Power Sources* **2001**, 100, 101.
- [65] R. K. Harris, E. D. Becker, S. M. Cabral de Menezes, R. Goodfellow, P. Granger, *Solid State Nucl. Magn. Reson.* **2002**, 22, 458.
- [66] S. Hayashi, K. Hayamizu, *Bull. Chem. Soc. Jpn.* **1989**, 62, 2429.
- [67] J. M. Whiteley, J. H. Woo, E. Hu, K.-W. Nam, S.-H. Lee, *J. Electrochem. Soc.* **2014**, 161, A1812–A1817.
- [68] S. S. Zhang, K. Xu, T. R. Jow, *J. Power Sources* **2004**, 138, 226.
- [69] J. M. Bray, C. L. Doswell, G. E. Pavlovskaya, L. Chen, B. Kishore, H. Au, H. Alptekin, E. Kendrick, M.-M. Titirici, T. Meersmann, M. M. Britton, *Nat. Commun.* **2020**, 11, 2083.
- [70] Y.-C. Hsieh, M. Leißing, S. Nowak, B.-J. Hwang, M. Winter, G. Brunklaus, *Cell Rep. Phys. Sci.* **2020**, 1, 100139.
- [71] Z. E. M. Reeve, C. J. Franko, K. J. Harris, H. Yadegari, X. Sun, G. R. Goward, *J. Am. Chem. Soc.* **2017**, 139, 595.

Manuscript received: February 7, 2022

Revised manuscript received: April 6, 2022

Accepted manuscript online: April 7, 2022

Version of record online: April 25, 2022